

A novel large displacement electrostatic actuator: pre-stress comb-drive actuator

This content has been downloaded from IOPscience. Please scroll down to see the full text.

2005 J. Micromech. Microeng. 15 1641

(<http://iopscience.iop.org/0960-1317/15/9/005>)

View [the table of contents for this issue](#), or go to the [journal homepage](#) for more

Download details:

IP Address: 140.113.38.11

This content was downloaded on 26/04/2014 at 11:39

Please note that [terms and conditions apply](#).

A novel large displacement electrostatic actuator: pre-stress comb-drive actuator

J C Chiou and Y J Lin

Department of Electrical and Control Engineering, National Chiao Tung University, Hsin-Chu, Taiwan, Republic of China

E-mail: chiou@cc.nctu.edu.tw and u8812808@cc.nctu.edu.tw

Received 25 January 2005, in final form 8 June 2005

Published 15 July 2005

Online at stacks.iop.org/JMM/15/1641

Abstract

This investigation proposes a novel large vertical displacement electrostatic actuator, called the pre-stress comb-drive actuator (PCA), which exhibits no pull-in and no hysteresis characteristics. The proposed PCA consists of a set of comb fingers fabricated along the composite beam and substrate. One end of the composite beam is clamped to the anchor, whereas the other end is elevated vertically by the residual stress. The actuation occurs when the electrostatic force, induced by the fringe effect, pulls the composite beam downward to the substrate. A post-heat treatment process was employed to increase the initial lift height of the PCA to obtain a large actuation stroke. A mathematical model, based on a newly developed modeling approach, is introduced to estimate the static characteristic of the PCA. A PCA was fabricated using the PolyMUMPs process based on the proposed design concept. Following packaging and applying a post-heat treatment process, a 110 μm initial tip height and a 90 μm vertical motion range were achieved. Neither pull-in nor hysteresis was observed. The simulation results were closely matched with the observations. This work also studies the frequency response and measurement of the maximum vibration of the PCA.

(Some figures in this article are in colour only in the electronic version)

1. Introduction

Micro-electro-mechanical systems (MEMS) enable suspended microstructures to be moved precisely and integrated with microelectronic circuits monolithically on a chip to perform or provide analog tuning or digital switching of linear or angular motion [1]. Various actuation mechanisms, such as thermal/bimetallic bimorph [1–3], electromagnetic [4, 5], piezoelectric [6, 7] and electrostatic actuation [8, 9], have been established and applied fundamentally in MEMS-based devices where mechanical actuation is required.

In MEMS research, the most widely used micro-actuator is the electrostatic actuator [10]. The main benefit of the electrostatic actuator is its characteristic small power consumption. Recently, various electrostatic actuator designs, such as the parallel plate, laterally comb drive and vertical comb-drive actuators, have been developed. The characteristic electrostatic force actuation between the parallel plates is proportional to the inverse of the square of the gap between the plates. The voltage-controlled parallel plate electrostatic

actuator exhibits a nonlinear phenomenon, called pull-in, which seriously constrains the stable region at one-third the length of the gap [11]. The lateral comb-drive structure has an advantage over such plate elements, in that the electrostatic force is independent of the displacement of the actuator. Consequently, the positioning of the comb-drive shuttle can be controlled accurately using the applied voltage. However, the shortcomings of comb actuators include a high driving voltage, a small displacement in dc driving mode and a large layout area. The vertical comb drive is considered to be regarded as the most feasible technique for obtaining a large angular motion. Here, the angular motion plays an important role in optical applications such as digital switching [12, 13] and raster scanning [14, 15]. Recently, a high aspect ratio micromachining process using electroplating, DRIE and ICP has been demonstrated to be important in further increasing an even larger angular motion [16]. Si dry etching is carried out from the top and bottom surfaces of the SOI wafer in constructing a vertical comb. The increase of the depth of backside Si etching increases the technical difficulty of

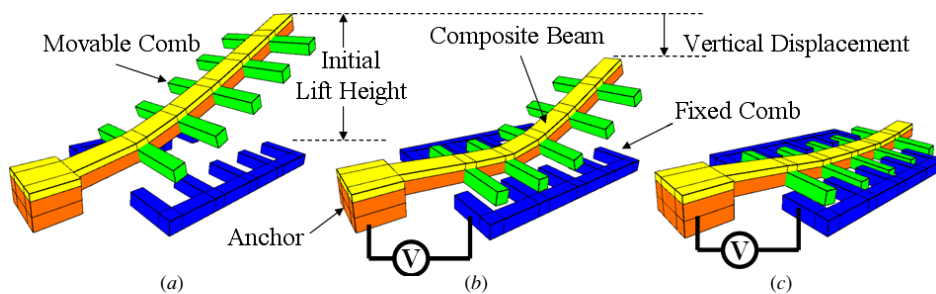


Figure 1. The PCA at different driving states; (a) initial state, (b) bias voltage state and (c) critical bias voltage state.

the method [17], and causes problems of alignment and gap expansion. Notably, a vertical comb-drive actuator cannot easily achieve a larger deflection angle at a low driving voltage.

The advantages of bulk micromachining, a MEMS fabrication technique, are in manufacturing flatter micromirrors, with high stiffness in the vertical direction and greater working space in the out-plane actuation. However, beam stiffness, isotropic/anisotropic bulk etching and electrical interconnect/isolation are difficult to control accurately. Surface micromachining provides a flexible mechanical and electrical structure. Here, the working/motion space of various actuators is limited in in-plane actuation or small out-plane motion displacement [14]. Chen *et al* used the stress-induced bending of a composite cantilever beam to raise a vertical mirror mounted on the free end [18]. A cantilever beam with a length of $1500\ \mu\text{m}$ with a $300\ \mu\text{m}$ vertical displacement is developed [18]. Its driving mechanism is similar to a parallel plate electrostatic actuator which has the drawback of pull-in, which limits its application to optical digital switching. The mechanical stability of the actuator becomes crucially essential when it is applied to other MEMS devices that require analog tuning. Rosa *et al* proposed an external electrode concept that contrasts with the conventional concept and frequently employed a parallel plate electrode scheme for the electrostatic actuation of MEMS devices [19]. The external electrode configuration allows the operation of electrostatic actuators to be controlled over their entire range of motion by preventing electrostatic pull-in instability. It is based on the application of the fringe effect between the moving electrode and the fixed external electrodes. Notably, the shape of the external electrodes seems to be arbitrarily designed. However, the fringe effect between the moving and fixed external electrodes is relatively inefficient. Accordingly, the static characteristic criteria in obtaining the actuating force of the electrostatic actuator are severely limited. Akiyama *et al* have demonstrated a comb-shape electrostatic actuator for high-speed feedback motion, with which they achieved almost $1\ \mu\text{m}$ stroke under $50\text{--}130\ \text{V}$ applied voltage when the initial height difference, due to the residual stress, was $2\ \mu\text{m}$ [20]. Note that the comb-shape electrostatic actuator was fabricated using metal and thick device layer of the SOI wafer that limits the initial height difference.

A novel pre-stress comb-drive actuator is developed to overcome the limitations of the actuation range of the aforementioned electrostatic actuator. The advantages of the pre-stress comb-drive actuator (PCA) include continuity of motion (without pull-in or hysteresis) and a large vertical

actuation range. A mathematical model is presented to predict the static characteristic of the PCA. A PCA was fabricated using the PolyMUMPs process based on the proposed design concepts. The static characteristic, frequency response and maximum vibration amplitude of the fabricated PCA were measured.

2. Principle

Figure 1 schematically depicts a PCA with different driven states. The PCA consists of an anchor, a composite beam and a set of comb fingers. These comb fingers, designed along the composite beam and substrate, acted as the movable and fixed comb fingers. Figure 1(a) shows one end of the composite beam, which is clamped to the anchor, while the other end is elevated due to the residual stress between the two deposited materials. Notably, the initial lift height of the PCA can be further enhanced by increasing the residual stress of the composite beam using a post-heat treatment process [18]. When a voltage, V , is applied between the movable and fixed comb, the movable composite beam can be pulled downward to the substrate by the electrostatic force induced by the fringe effect, as shown in figure 1(b). The taper-like distances between each movable and fixed comb are obtained from the free end to the fixed end based on the curved-up shape of the composite beam. In the actuating mechanisms, the movable comb fingers that are close to the anchor provide the main actuation force. As the actuation progresses, the retral movable comb fingers will be pulled down accordingly. As the driving voltage is increased, the vertical displacement of the free end of the PCA is increased. Notably, the electrostatic force is constrained when the movable comb finger is close to the fixed comb finger, independently of the input driving voltage. Therefore, the vertical electrostatic force approaches zero as the movable comb finger reaches its equilibrium position. Figure 1(c) demonstrates that, when a critical bias voltage is applied between the movable and fixed comb, the PCA will engage with the substrate.

3. Device modeling and simulation

To understand the properties of the PCA, a mathematical model based on composite beam theory, static electric field and decomposition analysis is used for modeling the static behavior of the PCA. In addition, a FEM simulator, IntelliSuite[®], was used to calculate the resonant frequencies and the corresponding solid mode shapes.

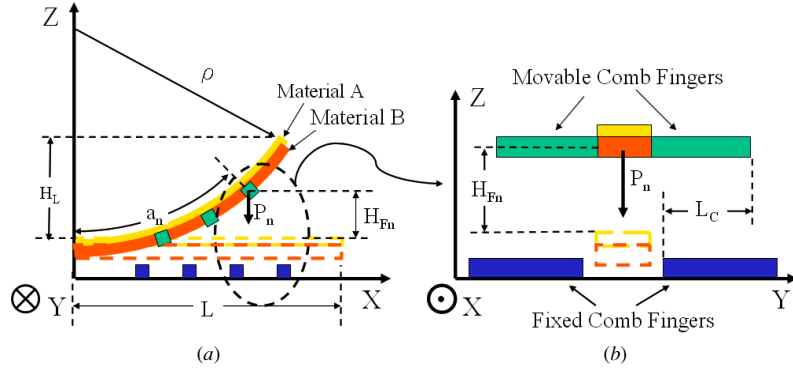


Figure 2. A schematic view of the PCA. (a) XZ plane cross-section view. The circle indicates a single pair of comb fingers. (b) YZ plane cross-section view.

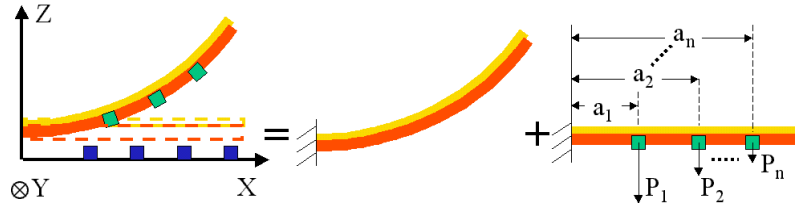


Figure 3. The schematic of the PCA separated into curvature composite beam and straight composite beam with taper multi-loadings.

3.1. The static behavior modeling and simulation

Based on the above-mentioned principle of the PCA, there are three modeling steps that need to be addressed: (1) illustrate the initial shape of the PCA; (2) calculate the electrostatic force in different electrical input signals and (3) obtain the displacement of the PCA by using the force balance equation. The details of these steps are discussed in the following sections.

3.1.1. Composite beam theory: curved-up shape calculation.

The PCA cantilever composite beam consisted of two materials A and B that possess tensile and compressed residual stresses, respectively, as shown in figure 2(a). With the released and heat treatment processes, the composite beam is assumed curving up a $1/\rho$ curvature with lift height, H_L , at the free end due to the induced stresses. In the present derivations, the symbols a_n , P_n , H_{Fn} and L are denoted as the distance related to the anchor, electrostatic force induced from the driving voltage, lift height of the n th movable comb finger and length of the composite beam, respectively. Here, one movable and two fixed comb fingers were defined as a single pair of comb fingers for the purpose of simulating and extracting capacitance function during the electrostatic force calculation. A cross-section view of the PCA is shown in figure 2(b), where L_C is the engaged length between the movable and fixed comb fingers.

Assuming that the movable and fixed comb fingers are completely parallel, i.e. neglecting deformation of the curved composite beam across the PCA width direction, the curvature of the PCA can be described by a one-dimensional differential equation [21]

$$\frac{1}{\rho} = \frac{z''}{[1 + (z')^2]^{3/2}} \quad (1)$$

where ρ is the radius of curvature, z is the deflection in the x direction, z' is the slope of the deflection curve and z'' is the displacement differential of z' . Furthermore, the curvature model of the composite beam can be expressed by [18]

$$\frac{1}{\rho} = \frac{6 \cdot (m \cdot \sigma_B - \sigma_A)}{h \cdot E_B \cdot \left[3 \cdot m + \frac{K}{q \cdot (1+q)^2} \right]} \quad (2)$$

where σ_A and σ_B are the residual stresses of materials A and B . E_A and E_B are Young's moduli of materials A and B , respectively. The symbols $m = \frac{E_A}{E_B}$, $q = \frac{t_A}{t_B}$ and K is denoted as

$$K = 1 + 4 \cdot m \cdot q + 6 \cdot m \cdot q^2 + 4 \cdot m \cdot q^3 + m^2 \cdot q^2 \quad (3)$$

where t_A and t_B are the thicknesses of materials A and B . K is a material coefficient of materials A and B . It is clear that the curvature of equation (2) is dependent on the residual stress, Young's modulus and thickness of composite materials A and B . Note that these parameters are controlled by the fabrication processes. Thus, if the process parameters are known, the initial lift height of the PCA can be designed in the early stages using equation (1).

3.1.2. PCA decomposition analysis. In this paper, a new modeling schematic is proposed to extract the vertical motion behavior of the PCA. Based on the direction integration method, the proposed PCA can be decomposed into a curvature composite beam and a strength composite beam with taper-like electrostatic forces in the length direction, as shown in figure 3. The curvature composite beam model is used to define the shape of the PCA, and the strength composite beam model is used to calculate the small deflection from the loads P_1 – P_n . Here, P_1 – P_n are the difference of the electrostatic force induced by the comb finger 1– n in the k th and $(k-1)$ th states. By separating the input signal into multiple sections, the small deflection in each state can be calculated. By adding up the small deflection of each section and the shape at the $(k-1)$ th state, we are able to obtain a new shape at the k th state.

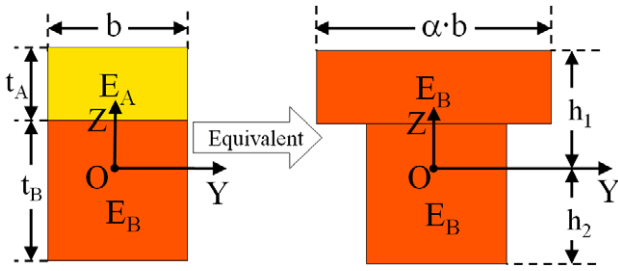


Figure 4. The equivalent beam model of the composite beam.

3.1.3. *Decomposition of multiple loads.* In the mechanics of material analysis, the deflection of a straight beam with constant multiple loads can be calculated as follows [21]:

$$\begin{cases} z_{xn} = \frac{P_n \cdot x^2}{6 \cdot E_c \cdot I_c} (3 \cdot a_n - x) \\ z'_{xn} = \frac{P_n \cdot x}{2 \cdot E_c \cdot I_c} (2 \cdot a_n - x) \end{cases}, \quad \text{for } 0 \leq x \leq a_n \quad (4)$$

$$\begin{cases} z_{xn} = \frac{P_n \cdot a_n^2}{6 \cdot E_c \cdot I_c} (3 \cdot x - a_n) \\ z'_{xn} = \frac{P_n \cdot a_n^2}{2 \cdot E_c \cdot I_c} \end{cases}, \quad \text{for } a_n \leq x \leq L \quad (5)$$

where x is the position of the beam, Z_{xn} is the shape of small deflection of the strength beam in the position x coming from the n th load, Z'_{xn} is the slope of shape in the position x coming from the n th load, a_n is the position of the n th load, P_n is the difference of the electrostatic force induced by the comb finger 1– n in the k th and $(k-1)$ th states, E_c is Young’s modulus of equivalent single material beam, and I_c is the moment of inertia of the equivalent single material beam. The following section discusses the equivalent material parameters and electrostatic force.

3.1.4. *Moment of inertia of composite beam.* In order to accurately calculate the moment of inertia of the designed beam, the composite beam can be recast into a T-shape single beam as shown in figure 4.

The material A with width b was replaced by material B with width $\alpha \cdot b$, where b is the width of the composite beam, α is the proportional constant between Young’s moduli of materials A and B, h_1 is the distance between the top side of material A and neutral axis of the T-shape beam and h_2 is the distance between the bottom side of material B and neutral axis of the T-shape beam. The moment of inertia of the T-shape beam can be expressed as [21]

$$I_c = \frac{1}{12} \cdot b \cdot t_A^3 + b \cdot t_A \cdot \left(h_1 - \frac{t_A}{2} \right)^2 + \frac{1}{12} \cdot (\alpha \cdot b) \cdot t_B^3 + \alpha \cdot b \cdot t_B \cdot \left(h_2 - \frac{t_B}{2} \right)^2 \quad (6)$$

where $E_c = E_B$, $\alpha = \frac{E_B}{E_A}$, $h_1 = \frac{t_A \cdot A_A + t_B \cdot A_B}{A_A + A_B}$, $h_2 = t_A + t_B - h_1$ and A_A and A_B are the cross-section areas of materials A and B, respectively.

3.1.5. *Extraction of the electrostatic force.* In general, the electrostatic force of a comb drive can be expressed as [22]

$$F_E = \frac{1}{2} \cdot N \cdot L_C \cdot \frac{dC}{dz} \cdot V^2 \quad (7)$$

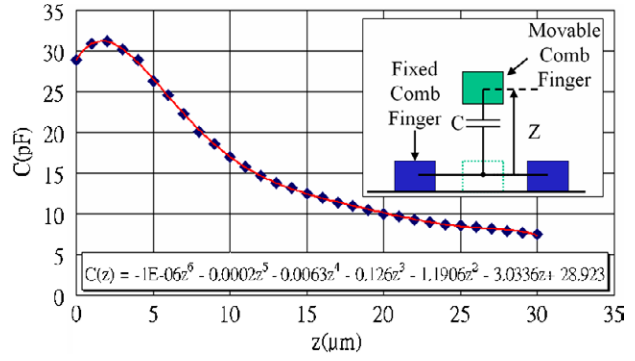


Figure 5. A capacitance versus displacement simulation of a single pair of comb drives.

where N is the number of comb fingers, L_C is the engaged length of comb fingers, dC/dz is the gradient of capacitance of comb fingers in the z motion direction and V is the applied dc bias voltage. In a static state case, N , L_C and V^2 are constant, and the dC/dz term, the electrostatic force index, is a function of z [23]. In order to extract the function accurately, electromagnetic simulation software AnSoft/Maxwell 2D was employed to calculate the comb finger capacitance at different z positions. By using Matlab simulation software, a sixth-order curve fitting was used to extract the capacitance function, $C(z)$, and the electrostatic force index was obtained by the derivative of the capacitance function. The electrostatic force can be rewritten as

$$F_{En}(z, V) = \frac{1}{2} \cdot N \cdot L_C \cdot (C_0 z^6 + C_1 z^5 + C_2 z^4 + C_3 z^3 + C_4 z^2 + C_5 z^1 + C_6) \cdot V^2 \quad (8)$$

where $F_{En}(z, V)$ is denoted as the unit electrostatic function of n th single pair of comb drives in the PCA. Since each movable comb finger has different positions, the electrostatic force contributed from each comb finger is experiencing taper-like behavior from fixed end to free end. Consequently, P_n is denoted as the difference of the electrostatic force induced by the comb finger 1– n in the k th and $(k-1)$ th states that can be expressed as

$$P_n = F_{En}(z, V_k) - F_{En}(z, V_{k-1}). \quad (9)$$

Figure 5 shows the simulation result of a single pair of comb drives. The simulation data are calculated by AnSoft/Maxwell 2D, and fit very well by the sixth-order polynomial, $C(z)$.

3.1.6. *Static simulation.* Table 1 presents the static analysis of the PCA with related simulation parameters. The shape of the PCA is determined by assuming the initial curvature of the composite beam. At a given curvature, a PCA is obtained with an initial lift height of 110 μm . The material properties in the present simulation were based on the reference from the MUMPS process [24].

Figure 6 reveals the primary simulation results of the PCA obtained by applying various voltages. Notably, the lift height is represented by the tip height at the free end of the PCA. Figure 6 clearly indicates that the typical pull-in behavior of parallel plate electrostatic actuators was not observed in the present design. Notably, in the early actuation stage, the electrostatic force obtained from the elevated comb fingers

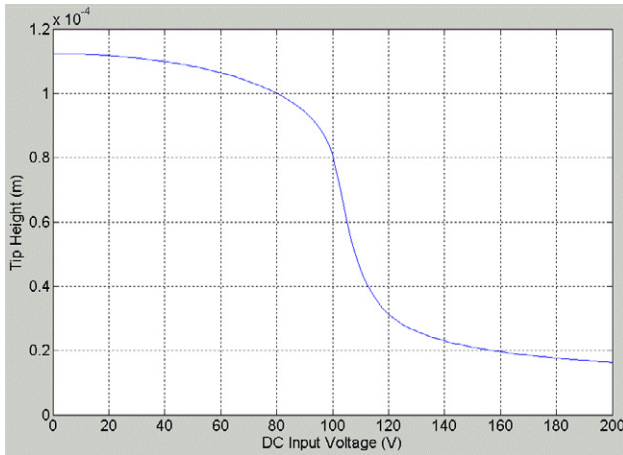


Figure 6. Steady-state simulation results of the PCA.

Table 1. The parameters table of primary simulation.

Symbol	Value	Symbol	Value
L	540 μm	t_A	0.5 μm
L_c	40 μm	t_B	1.5 μm
n	34	C_0	-1×10^{-18}
a_1-a_n	40–500 μm	C_1	-2×10^{-16}
ρ	1450 μm	C_2	-6×10^{-15}
b	40 μm	C_3	-1×10^{-13}
E_A	78 Gpa	C_4	-1×10^{-12}
E_B	160 Gpa	C_5	-3×10^{-12}
V	0–200 V	C_6	3×10^{-11}

overwhelms the spring force exerted in the composite beam, creating a steep gradient at certain applied voltages (80–120 V in the design herein). However, when most of the movable comb fingers made contact with the substrate at applied voltages higher than 120 V, the gradient variation becomes insignificant due to the decrease of effective comb fingers, as depicted in figure 1.

3.2. FEM mode simulation

To fully understand the resonant characteristics of the PCA, a FEM simulator, IntelliSuite[®], is used to calculate the resonant frequencies and the corresponding mode shapes. Note that in the present FEM simulations, we only require movable comb and composite beam to calculate the resonant frequencies. Table 2 shows the mode shape simulation results of the proposed PCA. In the first mode, there is an antinode in the free end (AN1) and a node in the fixed end (N1). Thus, the entire cross-section elements are actuated in the same direction. In the second mode, there are two nodes (N1 and N2) and two antinodes (AN1 and AN2). Thus, the AN1 and AN2 will experience an opposite motion during the actuation. In the third roll mode, attention must be paid to avoid shorting due to the contact between movable and fixed combs. In the fourth mode, three nodes (N1, N3 and N4) and three antinodes (AN1, AN3 and AN4) are observed in this simulation. In the fifth mode, the PCA is vibrating in the yaw motion. These simulation results can be used as the reference data in determining the resonant modes during the actual experimental measurements.

Table 2. The mode shape of the PCA.

Mode	Frequency (Hz)	Motion	Solid mode shape
First mode	5267.83	Pitch	
Second mode	32092.8	Pitch	
Third mode	80313.3	Roll	
Fourth mode	87555.2	Pitch	
Fifth mode	103654	Yaw	

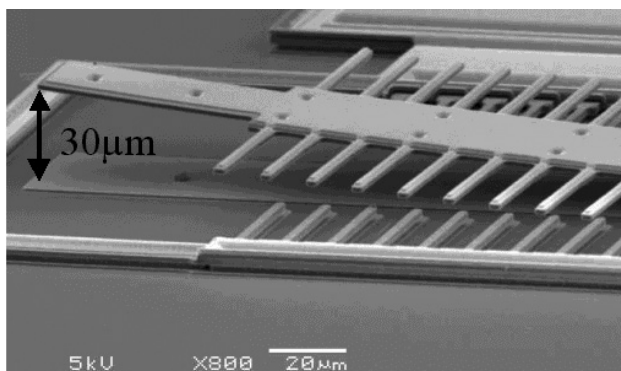


Figure 7. The SEM of a released PCA.

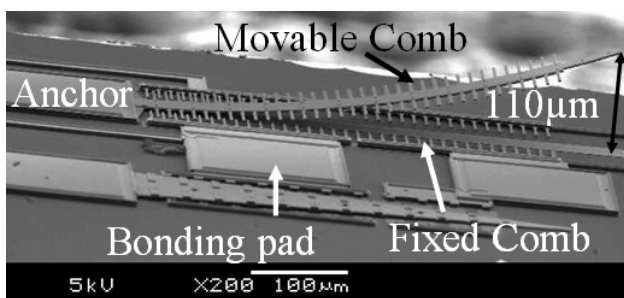


Figure 8. The SEM of the PCA after heat treatment process.

4. Fabrication

The proposed PCA is fabricated using the commercial available PolyMUMPs process [24]. This process consists of a nitride isolation layer, three polysilicon structural layers (Poly0 ~ 2), two phosphosilicon glass sacrificial layers (PSG1 & PSG2) and a gold metal layer (Au) for optical reflection and electronic connection. After the dicing process, hydrofluoric (HF) acid is used to release the MEMS structures.

The fabricated PCA consists of a $540 \times 40 \mu\text{m}^2$ composite beam that is fixed to an anchor structure with 34 movable comb fingers orthogonally mounted on the composite beam, and 35 fixed comb fingers are mounted on the surface of the nitride. Here the engaged length of the comb finger is designed to be $40 \mu\text{m}$. The composite beam is accomplished by depositing a $0.5 \mu\text{m}$ thick Au film on the surface of the $1.5 \mu\text{m}$ thick polysilicon (Poly2). Based on the tensile and compressed residual stresses of Au and Poly2 layers, the composite beam exhibited a curved up out of plane behavior. To prevent unnecessary residual stress on the movable comb fingers, Au film will not be deposited on top of the Poly2 layer of the movable comb fingers. The fixed comb fingers are manufactured by stacking up Poly0, PSG1, Poly1, PSG2 and Poly2. A scanning electron microscopy as shown in figure 7 is performed after the release process of the PCA is completed, where an initial height close to $30 \mu\text{m}$ is clearly observed. In order to enhance the initial lift height, the released PCA is placed on a hot plate at $150 \text{ }^\circ\text{C}$ for further heat treatment. Figure 8 demonstrates that the post-heat treatment will dramatically elevate the initial lift height of the PCA from $30 \mu\text{m}$ to $110 \mu\text{m}$ due to the increased residual stresses.

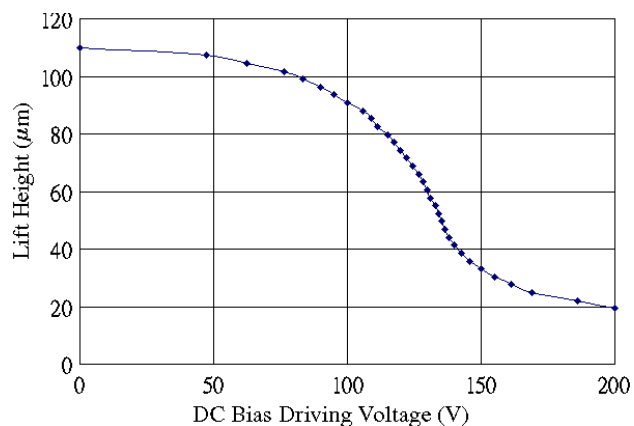


Figure 9. Static lift heights versus dc bias driving voltages.

5. Experiments and discussions

The released and post-processed PCA has been packaged using a dual-in-plane packaging (DIP). The microscope is used to measure the static characteristics and maximum resonant amplitudes of the PCA. Laser Doppler velocimetry (LDV) is a well-proven technique that can be used to measure the test specimen's velocity accurately and non-invasively. The relative displacement is obtained by integrating the velocity profile. Note that the present instrument cannot be used to measure the static object. In this work, LDV is used to measure the frequency response of the PCA.

5.1. Static characteristic measurement

The static characteristics of the PCA are obtained by applying a dc bias driving voltage at the fixed comb fingers by simultaneously tilting the packaged device for the ease of measurements and observations. The elevation of the PCA is measured by observing the overlapping images of the actuating cantilever beam and the meter ($2 \mu\text{m}$ resolution) existing in the eyepiece. In addition to the present setting, the large amplitude resonant frequencies and mode shapes can be easily observed.

The measured lift height versus the applied dc bias driving voltage between movable and fixed combs is completed and plotted in figure 9. The lift height is defined and measured at the free end of the PCA. Note that, compared to the simulation result in figure 6, the initial lift height ($V = 0$) is slightly different due to process tolerances (fabrication and heat treatment) and measurement error (tilt angle of device set-up). From the experiment and simulation results, we have observed that the tip of the free end will not make contact with the substrate due to the fact that we have designed a $70 \mu\text{m}$ length of the beam region without either movable or fixed comb fingers as shown in figure 7. A stable but nonlinear characteristic over the entire actuation range, i.e. $90 \mu\text{m}$ between 0 and 200 V, is obtained during this experiment. The typical pull-in and hysteresis behaviors of a parallel plate electrostatic actuator are not observed and matched well with the simulation result given in figure 6.

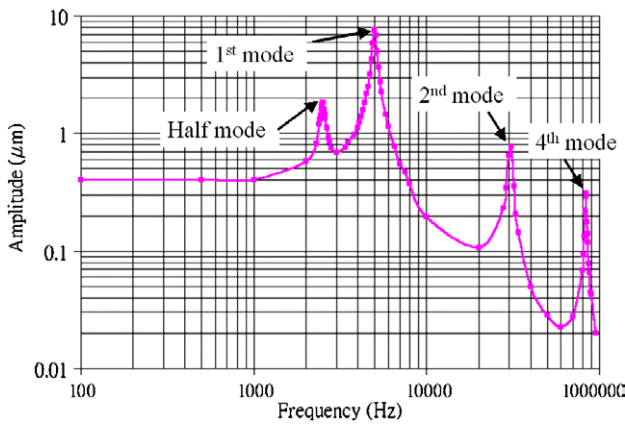


Figure 10. The frequency response of the PCA.

Table 3. The maximum vibration amplitude at different resonant frequencies.

Properties	Mode			
	Half	First	Second	Fourth
Frequency (measured) (Hz)	2487	4763	30120	84740
Frequency (simulated) (Hz)	N/A	5267.83	32092.8	87555.2
Driving voltage (V)	200	100	200	200
Amplitude (μm)	40	200	20	10

5.2. Frequency response measurement

As shown in figure 10, the frequency response of the PCA is obtained by using LDV. The PCA is biased by a sinusoidal wave with peak to peak voltages, 0–20 V, and frequency range between 100 Hz and 100 kHz. The first, second and fourth resonant frequency modes are measured at 5.01 kHz, 31 kHz and 84.03 kHz, respectively. The relative amplitude of the PCA remains the same for the frequency lower than 1 kHz. By increasing the frequency, the relative amplitudes of first, second and fourth resonant modes were about 20, 2 and 0.8 times that at frequency lower than 1 kHz. Note that third and fifth modes of fabricated PCA cannot be measured due to their lateral motion characteristics. Notably, a ‘half mode’ peak before the first mode peak resonance in 2487 Hz is also observed in this microscope measurement. This is also observed in different experiments without an exclusive discussion [18, 25, 26]. Jin *et al* have pointed out that the half mode characteristic is due to the double frequency and nonlinear effect in the electrostatic resonator [27].

5.3. Maximum vibration amplitude measurement

From a system design point of view, an actuator with reciprocation motion capability plays an important role in MEMS applications. In general, an actuator driving at resonant modes will have the advantages of large motion and low power consumption.

The maximum vibration amplitude at different resonant frequencies is measured and shown in table 3. The differences between different modes of the measured and the simulated values mainly come from fabricated variation and air damping.

The measured maximum vibration amplitude of half mode and first mode is close to $40 \mu\text{m}$ at 200 V and $200 \mu\text{m}$ at 100 V, respectively. Since the amplitude of the first mode is limited by the $110 \mu\text{m}$ initial lift height of the fabricated PCA, we are expecting to have higher amplitude if the substrate beneath the composite beam and movable comb can be removed completely.

6. Conclusion

This investigation describes a novel large displacement electrostatic actuator that exhibits no pull-in or hysteresis. A mathematical model, based on a newly developed modeling technique, is proposed to predict the steady static behavior of the PCA. FEM simulations are performed to determine the resonant frequencies and mode shapes of the designed PCA, which is fabricated using the PolyMUMPs process. The simulation results agree with the experimental data obtained using a microscope. The frequency response of the PCA is determined by LDV and a half mode is observed in this study. Although not reported herein, the nonlinearity and large driving voltage characteristics between the applied bias signal and the lift height can be improved by altering the lengths of the comb fingers. Notably, the lift height is approximately proportional to the square of the beam length [18]; increasing the length of PCA easily increases the initial lift height and thereby enhances the working distance of the PCA.

In the future, the PCA will be utilized to track and focus on the servo control of the optical pickup, exploiting its advantages of no pull-in, no hysteresis and a large displacement. In large projection display applications, a micromirror actuated by the PCA can be driven at its resonant frequency to obtain a large scanning angle with low power consumption.

Acknowledgments

This work was supported in part by Ministry of Economic Affairs, Taiwan, Republic of China under contract no. 91-EC-17-A-07-S1-0011, the National Science Council, Taiwan, Republic of China under contract no. NSC 93-2218-E-009-026 and by the Brian Research Center, University System of Taiwan, under grant 92B-711.

References

- [1] Mohamed A, Elsimar H and Ismail M 2003 Analysis, and optimization of a CMOS vertical thermal actuator *Proc. Symp. Design, Test, Integration and Packaging of MEMS/MOEMS* pp 214–7
- [2] Popa D O, Byoung H K, Wen J T, Stephanou H E, Skidmore G and Geisberger A 2003 Dynamic modeling and input shaping of thermal bimorph MEMS actuators *Proc. IEEE Int. Conf. on Robotics and Automation* vol 1 pp 1470–5
- [3] Tuantranont A and Bright V M 2002 Micromachined thermal multimorph actuators fabricated by multi-users MEMS process *Proc. IEEE Int. Conf. on Industrial Technology (IEEE ICIT '02)* vol 2 pp 941–4
- [4] Chowdhury S, Ahmadi M, Jullien G A and Miller W C 2000 A modular MEMS electromagnetic actuator for use in a hearing instrument *Proc. 43rd IEEE Midwest Symp. on Circuits and Systems* vol 1 pp 240–3

- [5] Ji C H, Kim Y K and Choi B K 2000 Design and fabrication of electromagnetic micromirror with bulk silicon mirror plate and aluminum spring *Proc. IEEE/LEOS Optical MEMS* pp 97–8
- [6] Park J Y, Yee Y J, Nam H J and Bu J U 2001 Micromachined RF MEMS tunable capacitors using piezoelectric actuators *Proc. IEEE Microwave Symp. Digest* vol 3 pp 2111–4
- [7] Haddab Y, Chaillet N and Bourjault A 2000 A microgripper using smart piezoelectric actuators *Proc. IEEE Int. Conf. on Intelligent Robots and Systems (IEEE/RSJ IROS)* vol 1 pp 659–64
- [8] Hung E S and Senturia S D 1999 Extending the travel range of analog-tuned electrostatic actuators *J. Microelectromech. Syst.* **8** 497–505
- [9] Mu X H, Kahrizi M and Landsberger L 2003 Design & fabrication of out-of-plane electrostatic actuators for optical application *Proc. IEEE Canadian Conf. on Electrical and Computer Engineering (IEEE CCECE)* vol 1 pp 133–6
- [10] Rosa M A, Dimitrijević S and Harrison H B 1998 Enhanced electrostatic force generation capability of angled comb finger design used in electrostatic comb-drive actuators *Electron. Lett.* **34** 1787–8
- [11] Pons-Nin J, Rodriguez A and Castaner L M 2002 Voltage and pull-in time in current drive of electrostatic actuators *J. Microelectromech. Syst.* **11** 196–205
- [12] Mita M, Miyauchi D, Toshiyoshi H and Fujita H 1998 An out-of-plane polysilicon actuator with a smooth vertical mirror for optical fiber switch application *Proc. IEEE/LEOS Summer Topical Meetings* pp II/33–34
- [13] Chen W C, Wu C Y and Lee C K 2003 Bi-directional movable latching structure using electrothermal V-beam actuators for optical switch application *Proc. IEEE/LEOS Optical MEMS* pp 149–50
- [14] Piyawattanametha W, Patterson P R, Dooyoung H, Toshiyoshi H and Wu M C 2003 A 2D scanner by surface and bulk micromachined vertical comb actuators *Proc. IEEE/LEOS Optical MEMS* pp 93–4
- [15] Conant R A, Nee J T, Lau K Y and Muller R S 2000 Dynamic deformation of scanning mirrors *Proc. Optical MEMS* pp 49–50
- [16] Chu C C, Tsai J M, Hsieh J and Fang W 2003 A novel electrostatic vertical comb actuator fabricated on [111] silicon wafer *Proc. IEEE MEMS-03* pp 56–9
- [17] Sasaki M, Briand D, Noell W and Rooij N D 2003 Vertical comb drive actuator constructed by buckled bridges in SOI-MEMS *Proc. IEEE/LEOS Optical MEMS* pp 89–90
- [18] Chen R T, Nguyen H and Wu M C 1999 A low voltage micromachined optical switch by stress-induced bending *Proc. IEEE MEMS '99* pp 424–8
- [19] Rosa M A, Bruyker D D, Volkel A R, Peeters E and Dunec J 2004 A novel external electrode configuration for the electrostatic actuation of MEMS based devices *J. Microelectromech. Syst.* **14** 446–51
- [20] Akiyama T, Stauffer U and Rooij N F 2000 Atomic force microscopy using an integrated comb-shape electrostatic actuator for high-speed feedback motion *Appl. Phys. Lett.* **76** 3139–41
- [21] Gere J M and Timoshenko S P 1990 *Mechanics of Materials* 3rd edn (Boston: PWS) 465, 772, and 301–8
- [22] Xie H and Fedder G K 2002 Vertical comb-finger capacitive actuation and sensing for CMOS-MEMS *Sensors Actuators A* **95** 212–21
- [23] Chiou J C and Lin Y J 2003 A new modeling method of vertical electrostatic comb drive *J. Comput. Eng. Sci.* **4** 641–4
- [24] Koester D A, Mahadevan R and Markus K W 1994 *MUMPS Introduction and Design Rules* MCNC MEMS Technology Applications Center
- [25] Lin H Y and Fang W 2000 Torsional mirror with an electrostatically driven lever-mechanism *Proc. IEEE/LEOS Optical MEMS* pp 113–4
- [26] Krishnamoorthy U, Lee D and Solgaard O 2003 Self-aligned vertical electrostatic combdrives for micromirror actuation *J. Microelectromech. Syst.* **12** 458–64
- [27] Jin Z, Wang Y, Xu Y and Ding C 1995 The properties of micromechanical resonator *Proc. 4th Int. Conf. Solid-State and Integrated Circuit Technology* pp 482–4